Angular Spectrum Representation of Pulsed Laser Beams with Two-Dimensional Smoothing by Spectral Dispersion

Pulsed laser beams with two-dimensional smoothing by spectral dispersion (2-D SSD), used in inertial confinement fusion (ICF), improve the on-target uniformity on the OMEGA laser system;[1–4] however, 2-D SSD is highly susceptible to significant amplitude modulation (AM) during its generation and propagation.[5–8] In addition to on-target uniformity, the smoothness of the pulsed beam as it propagates through the long laser amplifier chain is important because of the perennial concern regarding laser damage. Small-scale, nonlinear self-focusing can occur as the pulsed beam propagates through various optical components because of the large fluences inherent in ICF applications. Any AM, in space or time, present on the pulsed beam may induce self-focusing and lead to damage. OMEGA utilizes many spatial filters to help alleviate the buildup of high spatial frequencies that tend to self-focus. In an effort to reduce the overall AM, it is imperative that the AM produced by the SSD driver line is at an absolute minimum.

A complete analysis of the SSD driver line requires a model that accounts for diffraction and spatiotemporal spectral effects of the many optical components that comprise the driver during both the generation and propagation of 2-D SSD beams. AM sources and other nonideal behavior can occur at any point in the SSD driver line, and the impact of a particular optical component depends on its relative location and the parameters that describe the SSD operation. Laser beam propagation codes that include SSD as part of an entire ICF laser system modeling exist at other laboratories, for example, Prop92 at LLNL and Miró at CEA; however, they do not emphasize the underlying optical components in the SSD driver line. A comprehensive understanding of the AM issue and other nonideal behavior entails a rigorous examination of the specific optics involved in the SSD driver line, including the effects of multiple-layered dielectric media, crystal birefringence, multiple co-propagating beams, nonlinear grating behavior, and far-field distortion. A model must be able to simulate the nonideal effects, predict the relative impact, and characterize the behavior so that experimental measurements can be used to diagnose and excise the problem.

The code (Waasese) developed to address the AM issue in the SSD driver line simulates many optical components, predicts the degree of AM, and characterizes the AM mechanisms in terms of measurable signatures. Different AM sources are measured on near-field streak camera images and exhibit distinct spatiotemporal patterns, trends in the temporal spectrum, and/or AM that varies as a function of an SSD parameter. Waasese simulations associate these distinct characteristics or signatures to particular optic components. These signature/component relationships are then exploited to diagnose, locate, and eliminate the AM sources when used in conjunction with experimental measurements. Waasese has been successfully used to locate some AM sources and identify solutions in the new double-pass 2-D SSD driver line scheduled for installation on OMEGA. Waasese is based on the angular spectrum representation, which accurately models diffraction and spatiotemporal spectral effects. Waasese is not limited to AM issues and has been used to model observed far-field distortion. Waasese's inherent flexibility facilitates future enhancements as other laser propagation issues arise.

Waasese models the individual optical components of the SSD driver line using a transfer-function approach as opposed to applying the ideal spatiotemporal dependent phase term. An angular spectrum representation and/or a thin optic phase transformation describes the transfer functions of the optical components. This approach models SSD generation in a stepwise fashion so that nonideal components, such as wave plates, may be included at any point in the process such as in between the preshear and dispersion gratings. This is an important issue because the degree to which optical components contribute to AM depends on their relative location in the SSD driver line. For example, surface roughness of a far-field retro mirror of the second SSD dimension will produce AM on the first but not the second dimension because the second dimension has not been dispersed at this point. Also, the AM induced by the crystal birefringence of the second SSD dimension can be compensated, provided that re-imaging takes place prior to the final grating. Additional examples of the modeling capabilities of

Waasese include nonlinear behavior of gratings, multiple surface reflections from a crystal in combination with an end mirror that produce co-propagating beams with offset spatiotemporal spectra, angular-dependent phase modulation depth that produces distorted far-field spectra, multiple-layered dielectric coatings that model high-reflection (HR) or antireflection (AR) coatings, etalon effects that modulate the temporal spectrum, spatial phase modulation of irregular surfaces, and image rotation between grating pairs. Waasese is capable of modeling arbitrary initial spatial and temporal profiles such as Gaussian, hyperbolic tangent, square, round, and elliptical. A postprocessor for Waasese incorporates various instructional data-visualization techniques of the spatiotemporal intensity and phase history of 2-D SSD pulsed beams: a spatiotemporal cross section, a spatial cross section, a false-color instantaneous wavelength overlay, a time-averaged far-field view, and a time evolution of the far-field pattern. These data-visualization techniques provide valuable insight into various problems that arise and their subsequent solutions.

The angular spectrum representation provides a straightforward analytical and numerical method to accurately analyze the generation and propagation of 2-D SSD pulsed laser beams. The angular spectrum representation decomposes a pulsed beam into a continuous linear sum of harmonic plane waves that individually propagate with a unique direction and temporal frequency through the laser system. Each harmonic plane wave is completely described by three parameters: k_x, k_y, and ω. When the resultant harmonic plane waves are summed, a representation of a 2-D SSD pulsed laser beam is obtained that accurately models diffraction and spatiotemporal spectral effects. Certain optical components require a thin optic phase transformation operation, in real space, whenever the optical surfaces are not planar, e.g., lenses, irregular surfaces on mirror coatings, and surface roughness of optical finishing.

In this article we first describe the angular spectrum representation of the two main elements of the SSD operation used in Waasese: gratings and electro-optic (EO) phase modulators. We then apply these transfer functions to the ideal generation of 2-D SSD, which provides a foundation of comparison for the nonideal cases. Ideal 2-D SSD utilizes a linearized grating equation and a pure phase-modulation operation. Analytical expressions and Waasese demonstrate that the application of the ideal transfer functions reduces the problem to the well-known spatiotemporal-dependent phase term that describes 2-D SSD.[1,2] We also introduce the frequency domain and real-space data visualization capabilities of the Waasese postprocessor. Finally in a section covering nonideal 2-D SSD generation we discuss various errors and/or nonideal effects that include nonideal gratings, nonideal phase modulators, crystal birefringence, Littrow mount error, image rotation, temporal spectrum modulation, spatial spectrum modulation, and image-plane errors.

Angular Spectrum Representation

Consider the electromagnetic field of the pulsed laser beam that propagates along the beam axis $\hat{\mathbf{z}}$ within a nonmagnetic, nonconducting, source-free, linear, causal, spatially and temporally homogeneous, isotropic, and spatially and temporally locally linear dielectric medium described by a constant refractive index $n \equiv \sqrt{\mu\varepsilon/\mu_0\varepsilon_0}$. Let the electric field $\mathbf{E}'(\mathbf{r},t)$ of the pulsed laser beam be defined on an image plane at $z = z_0$:

$$\mathbf{E}_0{}'(\mathbf{r}_T,t) \equiv \mathbf{E}'(\mathbf{r},t)\Big|_{z=z_0}, \tag{1}$$

where the position vector and transverse position vector are defined, respectively, by

$$\mathbf{r} \equiv x\hat{\mathbf{x}} + y\hat{\mathbf{y}} + z\hat{\mathbf{z}} \tag{2}$$

and

$$\mathbf{r}_T \equiv x\hat{\mathbf{x}} + y\hat{\mathbf{y}} \tag{3}$$

in the right-handed rectangular coordinate system (x,*y*,*z*) with the corresponding unit vectors $(\hat{\mathbf{x}},\hat{\mathbf{y}},\hat{\mathbf{z}})$. In addition, let the pulsed laser beam possess the form of a modulated carrier of angular frequency ω_c:

$$\mathbf{E}_0{}'(\mathbf{r}_T,t) \equiv \mathbf{E}_0(\mathbf{r}_T,t)e^{i\omega_c t}, \tag{4}$$

where $\mathbf{E}_0(\mathbf{r}_T,t)$ is the spatiotemporal envelope of the pulsed beam. The angular spectrum of the electric field at the image plane is given by the forward, three-dimensional, spatial spatiotemporal Fourier-Laplace transform (compare Ref. 9, §5.1 and Ref. 10, Chap. 4):

$$\begin{aligned}\tilde{\mathbf{E}}_0(\mathbf{k}_T,\omega) &\equiv \tilde{\mathbf{E}}(\mathbf{k}_T,z_0,\omega)\\ &= \int_{-\infty}^{\infty}\!\!\int\!\!\int \mathbf{E}_0(\mathbf{r}_T,t)e^{i\omega t}e^{-i\mathbf{k}_T\cdot\mathbf{r}_T}\,dt\,dx\,dy.\end{aligned} \tag{5}$$

The wave vector and transverse wave vector are defined, respectively, as

$$\mathbf{k} \equiv k_x \hat{\mathbf{x}} + k_y \hat{\mathbf{y}} + k_z \hat{\mathbf{z}} \tag{6}$$

and

$$\mathbf{k}_T \equiv k_x \hat{\mathbf{x}} + k_y \hat{\mathbf{y}} \, , \tag{7}$$

where the transverse wave numbers or spatial frequencies k_x and k_y are real-valued and the longitudinal wave number k_z is given by the principle root of the expression

$$k_z \equiv \sqrt{k_0^2 n^2 - k_T^2} \, , \tag{8}$$

and $k_T^2 \equiv k_x^2 + k_y^2$. The quantity $k_0 \equiv 2\pi/\lambda = \omega'/c$ is the vacuum wave number, ω' is the angular frequency of the electromagnetic disturbance that is centered about the carrier ω_c,

$$\omega' \equiv \omega_c + \omega, \tag{9}$$

and $c \equiv 1/\sqrt{\mu_0 \varepsilon_0}$ is the vacuum speed of light.

Free-space propagation of the electric field of the pulsed laser beam along the beam axis in any source-free and homogenous region of dielectric is given exactly by the angular spectrum representation (compare Ref. 9, §5.1)

$$\mathbf{E}(\mathbf{r}_T, z, t) = \frac{1}{(2\pi)^3} \int\int\int_{-\infty}^{\infty} \tilde{\mathbf{E}}_0(\mathbf{k}_T, \omega) e^{i\Delta z k_z} e^{-i\omega t} e^{i\mathbf{k}_T \cdot \mathbf{r}_T} \, \mathrm{d}\omega \, \mathrm{d}k_x \mathrm{d}k_y \, , \tag{10}$$

where $\Delta z \equiv z - z_0$. The expression given in Eq. (10) is an exact solution to Maxwell's equations in an isotropic, source-free dielectric medium. Any inaccuracies associated with this method amount to assumptions made about the field behavior $\mathbf{E}_0(\mathbf{r}_T, t)$ on the initial plane $z = z_0$ (such as assuming scalar fields or Fresnel-Kirchoff boundary conditions) or when approximating the integrals as summations when performing numerical simulations. When $k_T^2 \le k_0^2 n^2$, the longitudinal wave number k_z is real-valued and the integrand of Eq. (10) represents homogenous plane waves with spectral amplitudes or angular spectra $\tilde{\mathbf{E}}_0(\mathbf{k}_T, \omega)$ whose phase fronts propagate in the direction given by the wave vector $\mathbf{k} \equiv k_x \hat{\mathbf{x}} + k_y \hat{\mathbf{y}} + k_z \hat{\mathbf{z}}$. Thus, the angular spectrum representation decomposes an arbitrary pulsed laser beam into a continuous sum of homogeneous plane waves that propagate in a unique direction and with an angular frequency ω'. The expression in Eq. (10) represents the general case of vectors and is certainly valid for each individual vector component; therefore it is applicable to the scalar diffraction problems presented in this article.

A useful measure that marks the boundary between the near field and far field for diffraction problems is the Rayleigh range given by (Ref. 11, p. 714)

$$z_R \equiv \frac{A}{\lambda_c} \, , \tag{11}$$

where A is the area of the beam (see Table 78.II for typical numbers on OMEGA). Another useful parameter is the Fresnel number given by

$$N \equiv \frac{a^2}{\lambda_c \Delta z} \, , \tag{12}$$

which measures the number of Fresnel zones contained within an aperture of width or diameter $2a$. For full-aperture illumination, the Fresnel number will determine the number of strong ripples apparent in the near-field diffraction pattern. However, a beam with a supergaussian profile or other rounded square shapes such as a hyperbolic-tangent will not exhibit these strong ripples (Ref. 11, p. 739). For this reason, the simulations presented here utilize these shapes to reduce the edge diffraction ripples in order to emphasize other diffraction effects. Waasese is based on the angular spectrum representation and is therefore inherently capable of modeling any beam shape or temporal profile.

Elements of the SSD Operation

The two basic elements of the SSD operation in terms of the angular spectrum representation—gratings and EO phase modulators—are presented as transfer functions in both real and frequency space to describe the complex 2-D SSD system as a set of interchangeable operations. This method also develops a sense of the resultant frequency-domain effects of each operation and its relation to the real space.

1. The Grating Equation

The grating equation relates an incident harmonic plane wave to a transmitted (or reflected) harmonic plane wave that is given by[12]

$$\sin(\theta_i) + \sin(\theta_t) = -m \frac{\lambda}{d} \, , \tag{13}$$

Table 78.II: The Rayleigh range Δz_R, the color-separation distance Δz_{crit}, and their ratio $\Delta z_{crit}/\Delta z_R$ for various beam diameters and two values of applied bandwidth for a dispersion of $d\theta_t/d\lambda$ = 197 μrad/Å and grating beam diameter $D_{grating}$ = 44 mm.

	Diameter (cm)								
	0.11	0.22	0.55	1.938	4.4	8.488	14.63	19.52	27.33
Δz_R (m)	0.902	3.608	22.55	280	1443	5371	15956	28405	55683
Δz_{crit} (m), 1.5 Å	0.186	0.745	4.653	57.77	297.8	1108.2	3292.4	5861.1	11489
$\Delta z_{crit}/\Delta z_R$	0.206	0.206	0.206	0.206	0.206	0.206	0.206	0.206	0.206
Δz_{crit} (m), 3.0 Å	0.093	0.372	2.327	28.89	148.9	554.12	1646.2	2930.6	5744.7
$\Delta z_{crit}/\Delta z_R$	0.103	0.103	0.103	0.103	0.103	0.103	0.103	0.103	0.103

where θ_i and θ_t are the incident and transmitted angles relative to the grating normal, m is the order of the grating, d is the groove spacing, $\lambda \equiv 2\pi c/\omega'$ is the wavelength, and $\omega' \equiv \omega_c + \omega$ is the angular frequency that is centered about the carrier ω_c. The gratings in the SSD driver lines at LLE are used in transmission mode with an order $m = -1$ (see Fig. 78.6). Solving Eq. (13) for θ_t with an order $m = -1$ yields

$$\theta_t = \sin^{-1}\left[\frac{\lambda}{d} - \sin(\theta_i)\right]. \tag{14}$$

Taking the derivative of Eq. (14) with respect to λ yields the grating dispersion

$$\frac{d\theta_t}{d\lambda} = \frac{1}{d\sqrt{1-\left[\frac{\lambda}{d} - \sin(\theta_i)\right]^2}} \ . \tag{15}$$

For the SSD laser systems at LLE, the gratings are typically in a Littrow mount, which is defined to be when the angles of the incident and transmitted plane waves are equal for a particular design wavelength, i.e., $\theta_{Litt} \equiv \theta_i = \theta_t$. Under this condition, an incident pulsed beam will retain its incident beam diameter and is described by

$$\sin(\theta_{Litt}) = \frac{\lambda_c}{2d} \ , \tag{16}$$

where $\lambda_c = 2\pi c/\omega_c$ is the central or design wavelength. Typically, the design parameters for a grating are the central wavelength λ_c and a desired amount of dispersion $d\theta_t/d\lambda$ while assuming a Littrow mount, which then determines the grating groove spacing d by substituting Eq. (16) into Eq. (15). Once a grating design is realized, an operating point has been determined on the $d\theta_t/d\lambda$ curve, which can be seen in the example illustrated in Fig. 78.7. When the bandwidth $\Delta\lambda$ that is induced by the SSD system is small enough, then the slope

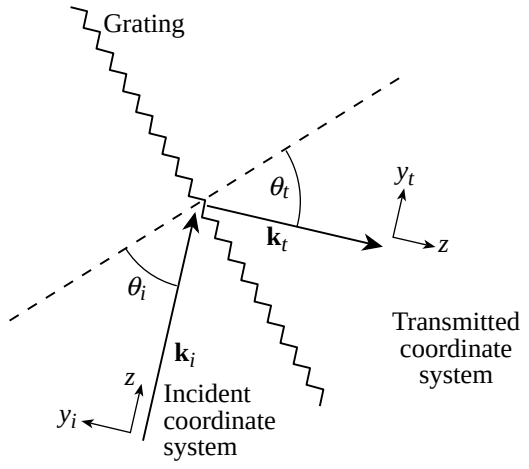

Figure 78.6
The coordinate systems for the incident and transmitted pulsed beams that traverse a grating in transmission mode of order $m = -1$. Notice that the beam axis (z) remains unaltered as a result of the grating operation; indicating the rotation from the incident to the transmitted coordinate system as the beam axis follows the course of the real beam.

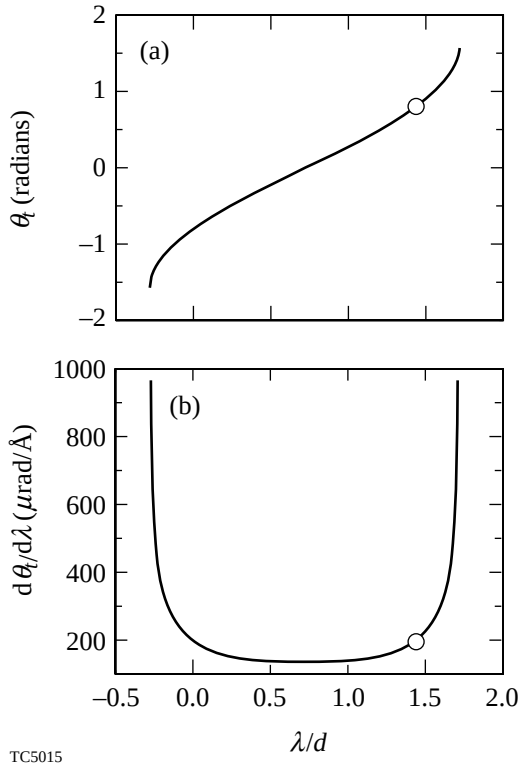

Figure 78.7
The design points on (a) the grating equation θ_t and (b) the grating dispersion equation $d\theta_t/d\lambda$ for λ_c = 1053 nm, $\theta_{L\,itt}$ = 46°, and d = 0.732 μm/groove.

$d\theta_t/d\lambda$ is nearly constant over that bandwidth; however, since Eq. (15) is inherently nonlinear, beam distortion becomes more significant as the bandwidth increases.

Consider an incident modulated pulsed laser beam with an angular carrier frequency of ω_c, pulse duration τ, and diameter D impinging upon a grating that disperses along the $\hat{\mathbf{y}}$ direction. Define the incident beam axis (z) to make an angle Θ_i with regard to the grating normal in the y-z plane. Then define a transmitted-beam axis that makes an angle Θ_t with regard to the grating normal. (This situation is illustrated in Fig. 78.6.) By decomposing the incident pulsed laser beam into its angular spectrum, the grating equation (14) may be used to accurately describe the action of the grating in the spatiotemporal frequency space. The grating acts as an angular transformation operation that redirects or maps each incident plane wave (completely described by the parameters k_x, k_y, and ω) onto the transmitted-beam axis. Notice that the image plane will be rotated onto the transmitted-beam axis as indicated in Fig. 78.6. Only the wave number in the $\hat{\mathbf{y}}$ direction is altered during this transformation, and, in general, the new transverse wave number is a function of both the transverse wave number and the angular frequency, i.e., $k_{y_g}\left(k_y,\omega\right)$. The transformation operation $k_{y_g}\left(k_y,\omega\right)$ is referred to as the grating angular dispersion, which acts along the $\hat{\mathbf{y}}$ direction as denoted by the subscript y. The grating angular dispersion may be expressed as [compare Eq. (14)]

$$k_{y_g}\left(k_y,\omega\right) = k_0 n \sin\left\{\Theta_t - \sin^{-1}\left[\frac{\lambda}{d} - \sin\left(\Theta_i + \sin^{-1}\left\{\frac{k_y}{k_0 n}\right\}\right)\right]\right\}, \qquad (17)$$

where $k_0 \equiv \omega'/c$, $\lambda \equiv 2\pi c/\omega'$, and $\omega' \equiv \omega_c + \omega$. The electric field of the transmitted pulsed laser beam is expressed, in general, by

$$E_g\left(\mathbf{r}_T,t\right) = \frac{1}{(2\pi)^3}\int\int\int_{-\infty}^{\infty} \tilde{E}_g\left(\mathbf{k}_T,\omega\right) e^{-i\omega t} e^{i\mathbf{k}_T\cdot\mathbf{r}_T}\, d\omega\, dk_x\, dk_y \qquad (18)$$

with the associated distorted angular spectrum given by

$$\tilde{E}_g\left(k_T,\omega\right) = \tilde{E}_0\left(k_x, k_{y_g}, \omega\right). \qquad (19)$$

The action of the grating may be interpreted as a nonlinear mapping of the angular spectrum onto a new spectral grid, which is nonuniform in general. Consequently, in general, Eq. (18) is not suitable for fast Fourier transform (FFT) algorithms, and a proper treatment requires a slow Fourier transform operation to regrid the data. Under certain approximations, however, Eq. (18) is suitable for FFT algorithms, which are then used to regrid the angular spectrum back onto the original grid: first, assuming that the angular dispersion is a linear function of the transverse wave number k_y and, second, assuming an additional linear dependence of the temporal frequency ω. Waasese can be configured to run in any of these three modes to calculate the grating effects where a tradeoff of speed versus accuracy must be made.

The first assumption may be expressed as a first-order Taylor series expansion about the transverse wave number k_y:

$$k_{y_g}\left(k_y,\omega\right) = k_{y_g}\left(k_y,\omega\right)\Big|_{k_y=0} + k_y \frac{\partial}{\partial k_y} k_{y_g}\left(k_y,\omega\right)\Big|_{k_y=0}. \qquad (20)$$

The partial derivative in Eq. (20) is given by

$$\frac{\partial}{\partial k_y} k_{y_g}\left(k_y,\omega\right) = \frac{\cos\left\{\Theta_t - \sin^{-1}\left[\frac{\lambda}{d} - \sin\left(\Theta_i + \sin^{-1}\left\{\frac{k_y}{k_0 n}\right\}\right)\right]\right\}}{\sqrt{1-\left[\frac{\lambda}{d} - \sin\left(\Theta_i + \sin^{-1}\left\{\frac{k_y}{k_0 n}\right\}\right)\right]^2}} \times \frac{\cos\left(\Theta_i + \sin^{-1}\left\{\frac{k_y}{k_0 n}\right\}\right)}{\sqrt{1-\left[\frac{k_y}{k_0 n}\right]^2}} . \quad (21)$$

If the grating is in the Littrow mount and is tuned to the center frequency ω_c, then evaluating the partial derivative at $k_y = 0$ yields

$$k_{y_g}\left(k_y,\omega\right)\Big|_{k_y=0} = k_0 n \sin\left\{\Theta_t - \sin^{-1}\left[\frac{\lambda}{d} - \sin\left(\Theta_i\right)\right]\right\} , \quad (22)$$

and while assuming that $\omega' \cong \omega_c$,

$$\frac{\partial}{\partial k_y} k_{y_g}\left(k_y,\omega\right)\Big|_{k_y=0} \cong 1. \quad (23)$$

Substituting Eqs. (22) and (23) into Eq. (20) gives

$$k_{y_g}\left(k_y,\omega\right) = \hat{k}_{y_g} + k_y , \quad (24)$$

where $\hat{k}_{y_g}(\omega) \equiv k_{y_g}(0,\omega)$. A change of variables defined by Eq. (24) yields [compare Eq. (18)]

$$E_g\left(\mathbf{r}_T,t\right) = \frac{1}{(2\pi)^3}\int\int\int_{-\infty}^{\infty}\left\{\tilde{E}_0\left(k_x,k_{y_g},\omega\right) \times e^{-i\omega t} e^{i\left[k_x x + k_{y_g} y - \hat{k}_{y_g}(\omega) y\right]}\right\} \mathrm{d}\omega\,\mathrm{d}k_x\,\mathrm{d}k_{y_g}. \quad (25)$$

Since $\hat{k}_{y_g}$ is only a function of the temporal angular frequency ω, the inverse 2-D spatial Fourier transform operation yields

$$E_g\left(\mathbf{r}_T,t\right) = \frac{1}{2\pi}\int_{-\infty}^{\infty}\tilde{E}_0\left(\mathbf{r}_T,\omega\right)e^{-i\omega t} e^{-i\hat{k}_{y_g}(\omega) y}\mathrm{d}\omega , \quad (26)$$

where

$$\tilde{E}_0\left(\mathbf{r}_T,\omega\right) = \frac{1}{(2\pi)^2}\iint_{-\infty}^{\infty}\tilde{E}_0\left(\mathbf{k}_t,\omega\right)e^{i\mathbf{k}_T\cdot\mathbf{r}_T}\mathrm{d}k_x\mathrm{d}k_y . \quad (27)$$

The distorted angular spectrum is then given by

$$\tilde{E}_g\left(\mathbf{k}_T,\omega\right) = \iint_{-\infty}^{\infty}\tilde{E}_0\left(\mathbf{r}_T,\omega\right)e^{i\hat{k}_{y_g}(\omega) y} e^{-i\mathbf{k}_T\cdot\mathbf{r}_T}\mathrm{d}x\mathrm{d}y = \int_{-\infty}^{\infty}\tilde{E}_0\left(k_x,y,\omega\right)e^{-i\hat{k}_{y_g}(\omega) y - ik_y y}\mathrm{d}y. \quad (28)$$

The utility of Eq. (28) lies in the ability to regrid the angular spectrum using conventional FFT algorithms. Waasese applies three operations to the initial angular spectrum $\tilde{E}_0\left(\mathbf{k}_T,\omega\right)$ to regrid the distorted angular spectrum $\tilde{E}_g\left(\mathbf{k}_T,\omega\right)$ onto the original numerical grid: inverse spatially transform the k_y dimension, apply the distortion term

$$e^{-i\hat{k}_{y_g}(\omega) y},$$

and, finally, forward spatially transform the y dimension.

The second assumption may be expressed as a bivariate, first-order Taylor series expansion:

$$k_{y_g}\left(k_y,\omega\right) = k_{y_g}\left(k_y,\omega\right)\Big|_{k_y=0,\omega=0} + k_y\frac{\partial}{\partial k_y}k_{y_g}\left(k_y,\omega\right)\Big|_{k_y=0,\omega=0} + \omega\frac{\partial}{\partial\omega}k_{y_g}\left(k_y,\omega\right)\Big|_{k_y=0,\omega=0}, \quad (29)$$

where $\omega' \equiv \omega_c + \omega$. The partial derivative with regard to ω in Eq. (29) is given by

$$\frac{\partial}{\partial\omega} k_{y_g}\left(k_y,\omega\right)$$

$$= \frac{1}{c}\sin\left\{\Theta_t - \sin^{-1}\left[\frac{\lambda}{d} - \sin\left(\Theta_i + \sin^{-1}\left\{\frac{k_y}{k_0 n}\right\}\right)\right]\right\}$$

$$+ k_0 n \frac{\cos\left\{\Theta_t - \sin^{-1}\left[\frac{\lambda}{d} - \sin\left(\Theta_i + \sin^{-1}\left\{\frac{k_y}{k_0 n}\right\}\right)\right]\right\}}{\sqrt{1-\left[\frac{\lambda}{d} - \sin\left(\Theta_i + \sin^{-1}\left\{\frac{k_y}{k_0 n}\right\}\right)\right]^2}}$$

$$\times \left[\frac{\lambda}{\omega' d} - \frac{\cos\left(\Theta_i + \sin^{-1}\left\{\frac{k_y}{k_0 n}\right\}\right)}{\sqrt{1-\left[\frac{k_y}{k_0 n}\right]^2}} - \frac{k_y}{k_0 \omega'}\right]. \quad (30)$$

If the grating is in a Littrow mount tuned to the center frequency ω_c, then

$$k_{y_g}\left(k_y,\omega\right)\Big|_{k_y=0,\omega=0} = 0, \quad (31)$$

$$\frac{\partial}{\partial k_y} k_{y_g}\left(k_y,\omega\right)\Big|_{k_y=0,\omega=0} = 1, \quad (32)$$

and

$$\frac{\partial}{\partial\omega} k_{y_g}\left(k_y,\omega\right)\Big|_{k_y=0,\omega=0} = \frac{1}{d\sqrt{1-\left[\frac{\lambda_c}{d} - \sin\left(\Theta_i\right)\right]^2}} \frac{\lambda_c}{c}. \quad (33)$$

Equation (29) can then be written as

$$k_{y_g}\left(k_y,\omega\right) = k_y + \xi_g \omega \quad (34)$$

and is known as the linearized grating angular dispersion, where Eq. (15) has been used in the definition

$$\xi_g \equiv \frac{\lambda_c}{c}\frac{\mathrm{d}\theta_t}{\mathrm{d}\lambda}\bigg|_{\omega=0,\theta_i=\Theta_i}.$$

The transmitted pulsed laser beam then becomes a temporally skewed or sheared version of the incident pulsed beam:

$$E_g\left(\mathbf{r}_T,t\right) = \frac{1}{2\pi}\int_{-\infty}^{\infty}\tilde{E}_0\left(\mathbf{r}_T,\omega\right)e^{-i\omega\left(t-\xi_g y\right)}\mathrm{d}\omega$$

$$= E_0\left(\mathbf{r}_T, t-\xi_g y\right), \quad (35)$$

where a temporal delay is imposed across the beam by an amount defined by

$$\tau_D = \xi_g D. \quad (36)$$

The angular spectrum is also sheared and is given by

$$\tilde{E}_g\left(\mathbf{k}_T,\omega\right) = \tilde{E}_0\left(k_x, k_y + \xi_g\omega, \omega\right). \quad (37)$$

During numerical simulations, Waasese regrids the initial angular spectrum $\tilde{E}_0\left(\mathbf{k}_T,\omega\right)$ using the technique described in association with Eq. (28).

2. The EO Phase Modulator

A strong microwave or radio frequency (RF) field inside a cavity resonator can modulate the optical refractive index of a nonlinear crystal such as lithium niobate ($LiNbO_3$).[13] The ideal EO phase modulator operates only in the time domain by applying the sinusoidal time-varying phase function $e^{i\delta_M \sin\left(\omega_M t\right)}$ to the optical electric field as

$$E_M\left(\mathbf{r}_T,t\right) = E_0\left(\mathbf{r}_T,t\right)e^{i\delta_M\sin\left(\omega_M t\right)}, \quad (38)$$

where δ_M is the modulation depth and $\upsilon_M \equiv \omega_M/2\pi$ is the RF modulation frequency. This modulation scheme is referred to as pure-tone phase modulation that is a specific type of a general class known as exponential or angle modulation and is inherently a nonlinear process. In general, the bandwidth applied by phase modulation has infinite extent, and discarding any portion will result in distortion and a degradation of signal fidelity, e.g., AM. Practically, the significant bandwidth applied by phase modulation is concentrated in a finite spectral region, which is a function of the modulation depth δ_M. The question then becomes How much bandwidth is required to retain adequate signal integrity? (See Carlson Ref. 14, pp. 239–245 for an in-depth discussion.)

The applied bandwidth is estimated by Carson's rule:

$$\Delta\upsilon = \frac{\Delta\omega}{2\pi} \approx 2\left(\delta_{\mathrm{M}} + 1\right)\upsilon_{\mathrm{M}} \ , \tag{39}$$

which appropriately goes to the limiting cases.

$$\Delta\upsilon = \begin{cases} 2\delta_{\mathrm{M}}\upsilon_{\mathrm{M}} & \delta_{\mathrm{M}} >> 1 \\ 2\upsilon_{\mathrm{M}} & \delta_{\mathrm{M}} << 1 \end{cases} ; \tag{40}$$

however, Carson's rule underestimates the bandwidth for the range $2 < \delta_{\mathrm{M}} < 10$. The bandwidth is more accurately estimated by

$$\Delta\upsilon \approx 2\left(\delta_{\mathrm{M}} + 2\right)\upsilon_{\mathrm{M}} \tag{41}$$

for modulation depths $\delta_{\mathrm{M}} > 2$. The applied bandwidth may also be expressed in terms of the wavelength as

$$\Delta\lambda = 2\left(\lambda_c - \frac{c}{\dfrac{c}{\lambda_c} - \dfrac{\Delta\upsilon}{2}}\right) \cong \frac{\Delta\upsilon\lambda_c^2}{c} \ , \tag{42}$$

where any estimate for $\Delta\upsilon$ can be applied. Typically, the estimate for the bandwidth given by $2\delta_{\mathrm{M}}\upsilon_{\mathrm{M}}$ is quoted in the literature on SSD applications (even for modulation depths $\delta_{\mathrm{M}} < 10$). This convention will be followed in this article for consistency not accuracy.

Equation (38) can be written as an equivalent series expansion given by (compare Ref. 14, p. 228)

$$E_{\mathrm{M}}\left(\mathbf{r}_T, t\right) = E_0\left(\mathbf{r}_T, t\right) \sum_{l=-\infty}^{\infty} J_l\left(\delta_{\mathrm{M}}\right) e^{il\omega_{\mathrm{M}}t} . \tag{43}$$

The spatiotemporal Fourier-Laplace transform of Eq. (43) yields the replicated angular spectrum

$$\tilde{E}_{\mathrm{M}}\left(k_T, \omega\right) = \tilde{E}_0\left(k_T, \omega\right) * \sum_{l=-\infty}^{\infty} J_l\left(\delta_{\mathrm{M}}\right) \delta\left(\omega - l\omega_{\mathrm{M}}\right) \ . \tag{44}$$

The original angular spectrum $\tilde{E}\left(k_T, \omega\right)$ is replicated with a spacing of ω_{M} and amplitudes determined by the Bessel functions of the first kind $J_l\left(\delta_{\mathrm{M}}\right)$ by virtue of the convolution process denoted in Eq. (44) by the symbol $*$. If the original bandwidth is not small compared to the modulation frequency, some overlap will exist from one band to the next. As long as the overlap is small, which is generally the case for well-defined systems, the spectral peaks will be well defined. Even if overlap does occur, it does not affect the validity of the linear superposition implied by Eq. (44). Figure 78.8(a) illustrates a spectrum obtained for a 1-ns pulse using the parameters $\delta_{\mathrm{M}} = 6.15$ and $\nu_{\mathrm{M}} = 3.3$ GHz.

Like any form of exponential modulation, pure-tone phase modulation possesses the unique property of constant amplitude. Maintaining a constant amplitude with a sinusoidal phase variation is best understood using a phasor interpretation where phasors for the carrier plus every sideband are vector-summed in phasor space as illustrated in Fig. 78.9. The resultant phasor sinusoidally sweeps back and forth (by an amount determined by the modulation depth δ_{M}) in phasor space while maintaining constant amplitude. All of the odd-order sideband pairs are in phase quadrature (due to the fact that the components of an odd-order pair have equal magnitude with opposite sign, i.e., $J_{-1}\left(\delta_{\mathrm{M}}\right) = (-1)^l J_l\left(\delta_{\mathrm{M}}\right)$ [see Ref. 15, p. 258, Eq. (9.1.5)], and all of the even-order sideband pairs

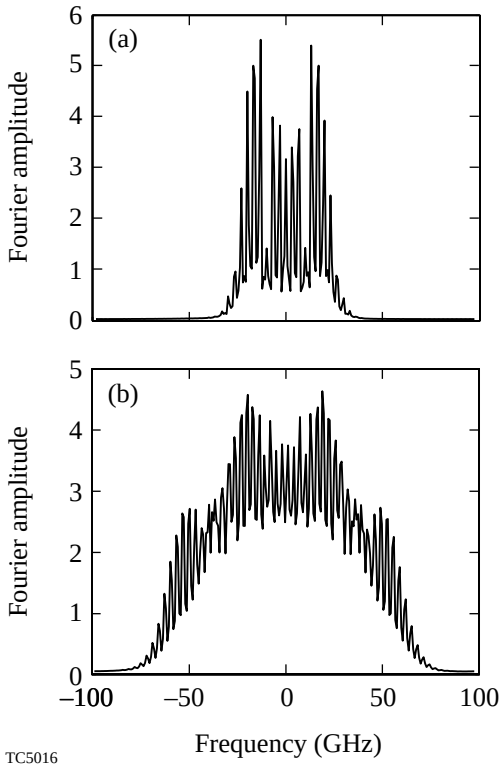

Figure 78.8
The temporal spectrum for (a) a pure-tone and (b) a two-tone phase-modulated optical pulse. The pulse duration is $\tau = 1$ ns and the parameters are $\delta_{\mathrm{M1}} = 6.15$, $\nu_{\mathrm{M1}} = 3.3$ GHz, $\Delta\lambda_{\mathrm{M1}} = 1.5$ Å, $\delta_{\mathrm{M2}} = 13.5$, $\nu_{\mathrm{M2}} = 3.0$ GHz, and $\Delta\lambda_{\mathrm{M2}} = 3.0$ Å.

are collinear with regard to the carrier. The odd-order pairs contribute to the desired sinusoidal phase modulation plus unwanted amplitude modulation. The even-order pairs compensate for the unwanted amplitude modulation imposed by the odd-order pairs (see pp. 230–233 of Ref. 14 for a complete discussion). The constant amplitude inherent in phase modulation relies on the delicate balance of the amplitudes and phases of its spectral components. Any deviation in this balance results in distortion that can exhibit itself as AM.

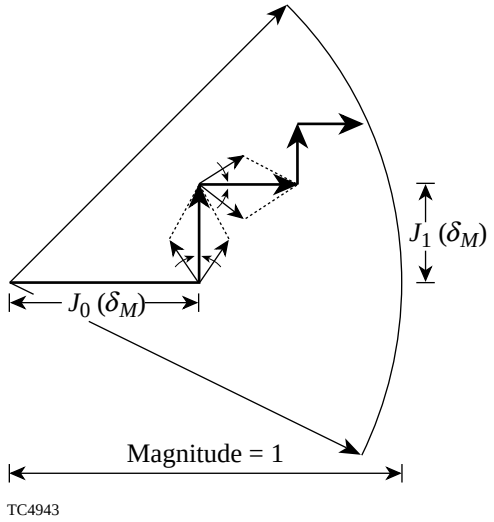

Figure 78.9
Phasor diagram of pure-tone phase modulation that depicts the phasor pairs for a small modulation depth. The diagram depicts how the even-order pairs compensate for the unwanted amplitude modulation imparted by the odd-order pairs. (Adapted from Ref. 14, p. 232, Fig. 6.7.)

Ideal 2-D SSD Generation

Here we describe the step-by-step process that Waasese uses to generate 2-D SSD. Ideal 2-D SSD is produced when the transfer functions given by Eqs. (37) and (44) are used. Analytical expressions are also developed and are shown to be equivalent to a generalization of Ref. 3, which includes beam shape. Ideal 2-D SSD is generated by a series of two ideal 1-D SSD operations performed on the two orthogonal transverse spatial directions of a seed-pulsed laser beam. Each 1-D SSD operation consists of an EO phase modulator sandwiched between a grating pair, such that an image plane exists at each grating plane. The angular spectrum representation of the grating and EO modulator, developed in the previous section, is drawn upon to illustrate the frequency-domain effects and how they relate to real space.

1. 1-D SSD Operation

Since each of the gratings is assumed to be at an image plane, this implies that some kind of image-relaying system must be in place. For practical SSD systems, these are afocal image relay telescopes with slow lenses that do not contribute significant aberrations. Figure 78.10 depicts the 1-D SSD

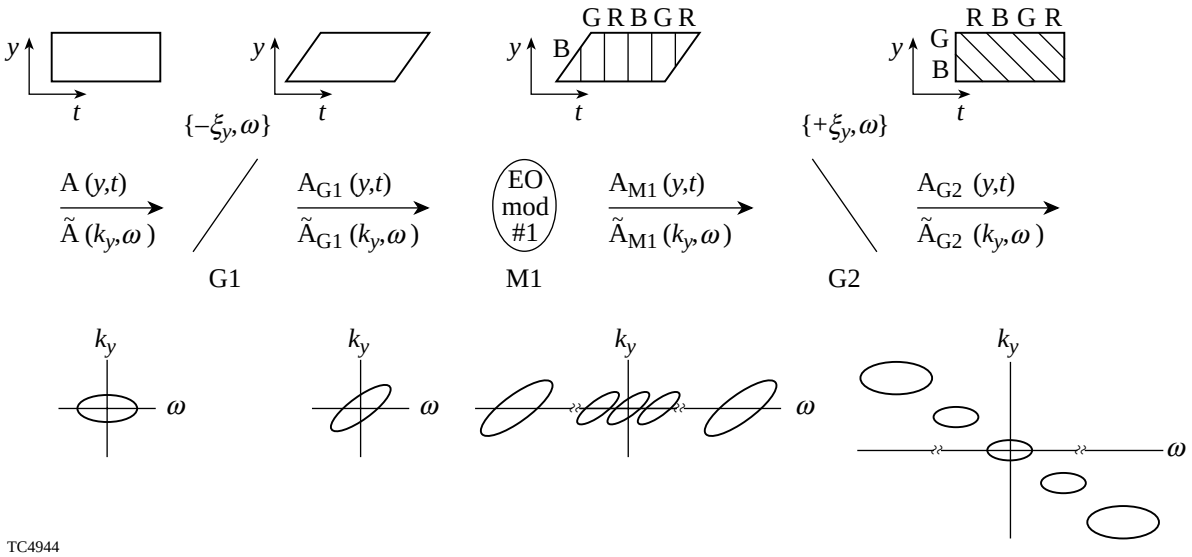

Figure 78.10
A schematic representation of the 1-D SSD operation showing the two important functions: gratings and EO phase modulator. In addition, the image planes are indicated along with the function names and a rough sketch of the field shape, in both real and frequency space, after each operation.

operation with the three major components, including the field names at certain locations. If the bandwidth $\Delta\lambda$ (typically 1 Å $< \Delta\lambda <$ 12 Å) introduced by the SSD system is small relative to the operating wavelength λ_c (for OMEGA the IR wavelength is 1053 nm), then the linearized grating angular dispersion Eq. (34) is an adequate representation of the grating and serves this section by demonstrating the ideal or desired response of an SSD system.

Consider a seed-modulated pulsed laser beam with an angular carrier frequency of ω_c, pulse duration τ, and diameters D_y and D_x. The electric field is defined on an image plane as $E_0(\mathbf{r}_T, t)$ with the associated angular spectrum $\tilde{E}_0(\mathbf{k}_T, \omega)$ and is image relayed onto the input of grating G1. Let the first grating G1 preshear the pulsed beam with a linearized angular dispersion of $-\xi_y$ along the $\hat{\mathbf{y}}$ direction. Consequently, the sheared field after the grating G1 is given by [compare Eq. (35)]

$$E_{\mathrm{G1}}(\mathbf{r}_T, t) = E_0(\mathbf{r}_T, t + \xi_y y), \tag{45}$$

where a temporal delay is imposed across the field by an amount given by $\tau_{D_y} = \xi_y D_y$. The angular spectrum is also sheared and is given by [compare Eq. (37)]

$$\tilde{E}_{\mathrm{G1}}(\mathbf{k}_T, \omega) = \tilde{E}_0(k_x, k_y - \xi_y\omega, \omega), \tag{46}$$

where the angular spectrum has been distorted only in the direction parallel to the k_y axis by the quantity $\xi_y\omega$. A representation of the sheared field and angular spectrum is illustrated in Fig. 78.10. Let the EO phase modulator have a modulation depth of δ_{M1} and a RF modulation frequency of $\upsilon_{\mathrm{M1}} = \omega_{\mathrm{M1}}/2\pi$. By combining the results from Eqs. (43) and (45), the electric field becomes

$$\begin{aligned} E_{\mathrm{M1}}(\mathbf{r}_T, t) &= E_{\mathrm{G1}}(\mathbf{r}_T, t) e^{i\delta_{\mathrm{M1}}\sin(\omega_{\mathrm{M1}}t)} \\ &= E_{\mathrm{G1}}(\mathbf{r}_T, t) \sum_{l=-\infty}^{\infty} J_l(\delta_{\mathrm{M1}}) e^{il\omega_{\mathrm{M1}}t} \end{aligned} \tag{47}$$

and the replicated-sheared angular spectrum is given by

$$\tilde{E}_{\mathrm{M1}}(\mathbf{k}_T, \omega) = \tilde{E}_{\mathrm{G1}}(\mathbf{k}_T, \omega) * \sum_{l=-\infty}^{\infty} J_l(\delta_{\mathrm{M1}}) \delta(\omega - l\omega_{\mathrm{M1}}). \tag{48}$$

A representation of the phase-modulated sheared field and angular spectrum is illustrated in Fig. 78.10. The second grating G2 now acts to disperse the increased bandwidth and remove the preshear from the first grating G1. Let the linearized angular dispersion be of equal magnitude and in the same direction as the first grating but with opposite sign, i.e., $+\xi_y$ (this is realized through the image flip of an odd number of image relays), so that the electric field becomes

$$E_{\mathrm{G2}}(\mathbf{r}_T, t) = E_{\mathrm{M1}}(\mathbf{r}_T, t - \xi_y y), \tag{49}$$

and the unsheared angular spectrum is given by

$$\tilde{E}_{\mathrm{G2}}(\mathbf{k}_T, \omega) = \tilde{E}_{\mathrm{M1}}(k_x, k_y + \xi_y\omega, \omega). \tag{50}$$

After substituting the results of Eqs. (45)–(47)

$$\begin{aligned} E_{\mathrm{G2}}(\mathbf{r}_T, t) &= E_{\mathrm{G1}}(\mathbf{r}_T, t - \xi_y y) e^{i\delta_{\mathrm{M1}}\sin\left[\omega_{\mathrm{M1}}(t+\xi_y y)\right]} \\ &= E_0(\mathbf{r}_T, t) e^{i\delta_{\mathrm{M1}}\sin\left[\omega_{\mathrm{M1}}(t+\xi_y y)\right]} \\ &= E_0(\mathbf{r}_T, t) \sum_{l=-\infty}^{\infty} J_l(\delta_{\mathrm{M1}}) e^{il\omega_{\mathrm{M1}}(t+\xi_y y)}. \end{aligned} \tag{51}$$

The angular spectrum of the 1-D SSD operation is then given by the spatiotemporal Fourier-Laplace transform of Eq. (51):

$$\begin{aligned} \tilde{E}_{\mathrm{G2}}(\mathbf{k}_T, \omega) &= \tilde{E}_0(\mathbf{k}_T, \omega) \\ &\quad * \sum_{l=-\infty}^{\infty} J_l(\delta_{\mathrm{M1}}) \delta(k_x, k_y - l\xi_y\omega_{\mathrm{M1}}, \omega + l\omega_{\mathrm{M1}}), \end{aligned} \tag{52}$$

where it is important to notice that exact replicas of the original spectrum, modified only by the amplitude of the Bessel functions of the first kind $J_l(\delta_{\mathrm{M1}})$, are centered on a regularly spaced line or comb of delta functions described by the summation operation. The comb of delta functions lies along the line $k_y = \xi_y\omega$ on the $k_y - \omega$ plane of the 3-D spatiotemporal spectrum and are spaced by $\xi_y\omega_{\mathrm{M1}}$ on the k_y axis and ω_{M1} on the ω axis. A representation of the final field and angular spectrum is illustrated in Fig. 78.10. Each replica of the original angular spectrum in Eq. (52) can be interpreted as an individual colored-pulsed beam with an associated wavelength or color $\lambda \equiv 2\pi c/\omega'$, where $\omega' = \omega_c + l\omega_{\mathrm{M1}}$, whose phase front advances in the direction $\mathbf{k} \equiv k_x\hat{\mathbf{x}} + (k_y - l\xi_y\omega_{\mathrm{M1}})\hat{\mathbf{y}} + k_z\hat{\mathbf{z}}$.

It is important to notice that, for propagation distances $\Delta z << z_R$ (such that minimal edge diffraction takes place for rounded square beams), the individual colored-pulsed beams retain their shape and continue to propagate along the beam axis and only the phase fronts break across the beam in a different direction. The individual colored beams will eventually separate since the energy flows along the direction **k**. The distance that colored-pulsed beam shifts in the transverse direction is given approximately by

$$\Delta y_l = \Delta z \tan\left(\Delta\theta_l\right), \tag{53}$$

where

$$\Delta\theta_l = \xi_g \frac{c}{\lambda_c} \Delta\lambda_l \frac{D_{\text{grating}}}{D}, \tag{54}$$

$\Delta\lambda_l \cong \left(\lambda_c^2/c\right) l \nu_{\text{M1}}$ is the spectral offset of a particular color, and D_{grating} is the beam diameter at the grating. The critical propagation distance for color separation is defined as when the outermost colored-pulsed beam has shifted by one beam diameter, i.e., $\Delta y = D_y$, and is approximated by

$$\Delta z_{\text{crit}} = \frac{D_y}{\tan(\Delta\theta)} \cong \frac{D_y}{\Delta\theta} = \frac{2}{\xi_g} \frac{\lambda_c}{c\Delta\lambda} \frac{{D_y}^2}{D_{\text{grating}}}, \tag{55}$$

where $\Delta\lambda$ is the applied bandwidth given by Eq. (42). The data in Table 78.II represents Δz_{R}, Δz_{crit}, and $\Delta z_{\text{crit}}/\Delta z_{\text{R}}$ for various OMEGA beam diameters for the system parameters: $\mathrm{d}\theta_t/\mathrm{d}\lambda\big|_{\omega=0} = 197\ \mu$rad/Å, $\Delta\lambda_{\text{M1}} = 1.5$ Å, 3.0 Å, and $D_{\text{grating}} = 44$ mm.

The electric field of a pulsed beam is a complex three-dimensional object whose intensity distribution, in space, is suitably described as a *brick of light* that moves along the propagation axis at the group velocity of the pulse. At one position of the propagation axis, the intensity of the brick of light is distributed about the transverse spatial dimensions as described by the beam profile and in time as described by the pulse shape. Taking different kinds of cross sections or slices of the brick of light is a way to visualize the multidimensioned data. A spatiotemporal cross section illustrates the intensity history of the pulsed beam. As an example, a spatiotemporal slice of a 1-D SSD pulsed laser beam is shown in Fig. 78.11 for two orthogonal directions with the system parameters $\delta_{\text{M1}} = 6.15$, $\nu_{\text{M1}} = 3.3$ GHz, $\Delta\lambda_{\text{M1}} = 1.5$ Å, $\tau = 1$ ns, $D_y = D_x = 44$ mm, and where stepped hyperbolic-tangent profiles were used in the spatial and temporal dimensions. In addition a false-color representation of the instantaneous wavelength is defined by

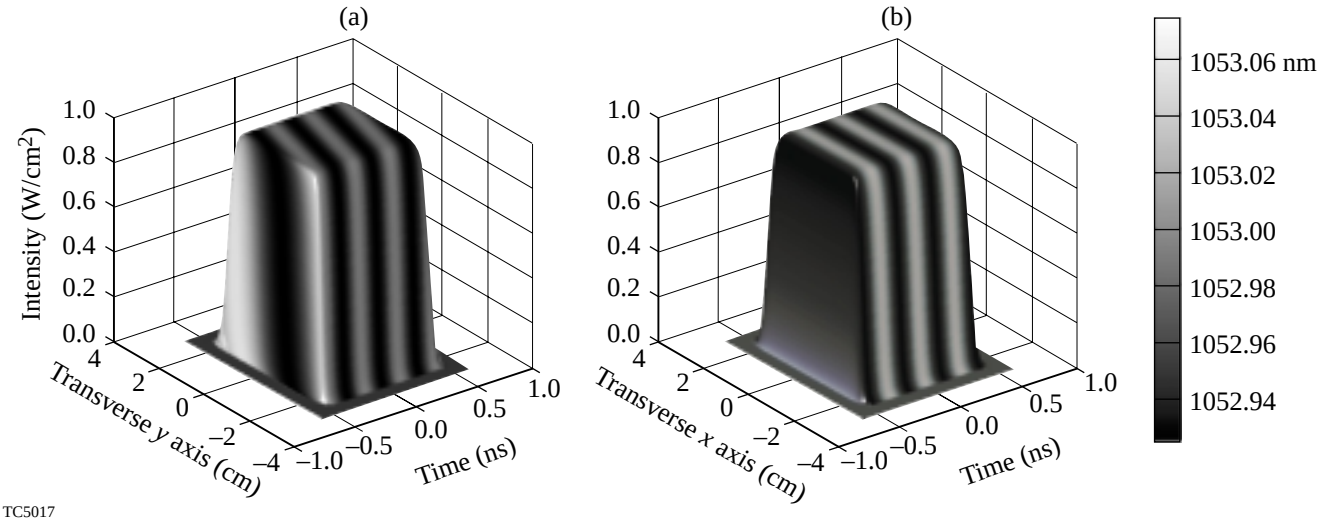

Figure 78.11
Spatiotemporal slices along (a) the *y*-*t* plane and (b) the *x*-*t* plane of a 1-D SSD pulsed beam with an overlay of the instantaneous wavelength $\hat{\lambda}\left(\mathbf{r}_T, t\right)$ superimposed onto the intensity profile for the system parameters $\delta_{\text{M1}} = 6.15$, $\nu_{\text{M1}} = 3.3$ GHz, $\Delta\lambda_{\text{M1}} = 1.5$ Å, $\tau = 1$ ns, $N_{c_y} \cong 1$, $\tau = 1$ ns, $D_y = D_x = 44$ mm, and where hyperbolic-tangent profiles were used in the spatial and temporal dimensions.

$$\hat{\lambda}(\mathbf{r}_T,t) \equiv \frac{c}{\frac{c}{\lambda_c} - \hat{\nu}} \ , \tag{56}$$

where the instantaneous frequency is given by

$$\hat{\nu} \equiv \frac{1}{2\pi}\frac{\partial \varphi}{\partial t} \tag{57}$$

and φ is the instantaneous phase of the field of the form $e^{i\varphi(y,t)}e^{i\omega_c t}$. The instantaneous wavelength is shown mapped onto the 3-D intensity surface, in effect, displaying the phase information of the electric field as a fourth dimension of data. The resultant dispersed spectrum of the 1-D SSD operation is displayed across the beam as one cycle of instantaneous wavelength or color, i.e., every color is displayed twice as the RF phase modulation cycles through 2π radians. In general, the fraction of RF phase-modulation cycles completed during the temporal shear $\tau_{D_y} = \xi_y D_y$, imposed by the first grating G1, and displayed across the beam as a result of the second grating G2, is determined by the number of color cycles (compare to Ref. 1):

$$N_{c_y} \equiv \tau_{D_y} \nu_{\mathrm{M1}} \, . \tag{58}$$

The instantaneous wavelength (or color) is not to be confused with the discrete colored-pulsed beams mentioned in the previous paragraph; the instantaneous wavelength is a continuous function defined in the temporal domain, whereas the other forms a discrete set defined in the temporal frequency domain. The bandwidth of the instantaneous frequency is given by

$$\Delta\hat{\nu} \equiv 2\delta_{\mathrm{M1}}\nu_{\mathrm{M1}} \, . \tag{59}$$

Notice that no approximation is made here as compared to the frequency-domain bandwidth described by Eqs. (39) and (41), and that it equals the bandwidth in the limit of large modulation depths given by Eq. (40). This fact illustrates the important difference between the instantaneous frequency and that of the frequency domain. When used with care, however, the instantaneous frequency is useful in describing some optical effects (such as etalons) since the modulation rate is slow compared to the underlying optical carrier. Another very important difference is that $\hat{\lambda}(\mathbf{r}_T,t)$ is a smooth, continuous function, and the frequency-space spectrum is comprised of a discrete set of frequencies (broadened only by the finite duration of the pulse width) as described by Eq. (44).

2. Series of Two 1-D SSD Operations

Consider, in a manner analogous to the previous subsection, a seed-modulated pulsed laser beam with an angular carrier frequency ω_c, pulse duration τ, and diameters D_y and D_x. The electric field is defined on an image plane as $E_0(\mathbf{r}_T,t)$ with the associated angular spectrum $\tilde{E}_0(\mathbf{k}_T,\omega)$ and is image relayed onto the input of grating G1. A diagram of the 2-D SSD system is shown in Fig. 78.12. Let the first SSD operation be given by Eqs. (51) and (52). Let the first grating of the second-dimension G3 operation preshear the pulsed beam with a linearized angular dispersion of $-\xi_x$ along the direction $\hat{\mathbf{x}}$. Consequently, the sheared field after the grating G3, in terms of the results from the first dimension Eq. (35), is given by

$$E_{\mathrm{G3}}(\mathbf{r}_T,t) = E_{\mathrm{G2}}(\mathbf{r}_T, t+\xi_x x) \ , \tag{60}$$

where a temporal delay imposed across the field is an amount given by $\tau_{D_y} = \xi_x D_x$. The sheared angular spectrum is given by [compare Eq. (37)]

$$\tilde{E}_{\mathrm{G3}}(\mathbf{k}_T,\omega) = \tilde{E}_{\mathrm{G2}}(k_x - \xi_x\omega, k_y, \omega), \tag{61}$$

where the angular spectrum has been distorted only in the direction parallel to the k_x axis by the quantity δ_{M2}. Let the second EO phase modulator have a modulation depth of δ_{M2} and a RF modulation frequency of $\upsilon_{\mathrm{M2}} = \omega_{\mathrm{M2}}/2\pi$. The electric field becomes

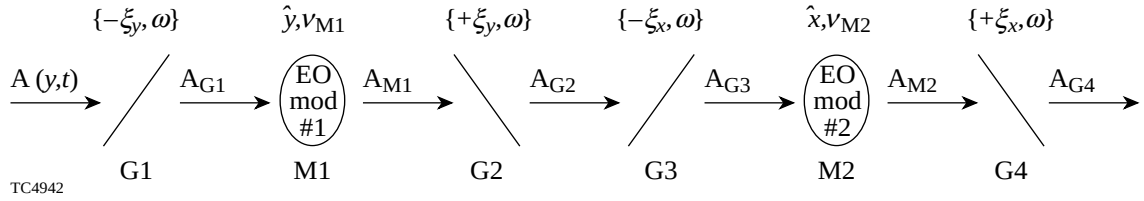

Figure 78.12
A schematic representation of the 2-D SSD operation, which exhibits a series of two 1-D SSD operations that act on two orthogonal directions $\hat{\mathbf{x}}$ and $\hat{\mathbf{y}}$.

$$E_{\mathrm{M2}}(\mathbf{r}_T,t) = E_{\mathrm{G3}}(\mathbf{r}_T,t)e^{i\delta_{\mathrm{M2}}\sin(\omega_{\mathrm{M2}}t)}$$
$$= E_{\mathrm{G3}}(\mathbf{r}_T,t)\sum_{m=-\infty}^{\infty} J_m(\delta_{\mathrm{M2}})e^{im\omega_{\mathrm{M2}}t}, \quad (62)$$

and the replicated-sheared angular spectrum is given by

$$\tilde{E}_{\mathrm{M2}}(\mathbf{k}_T,\omega) = \tilde{E}_{\mathrm{G3}}(\mathbf{k}_T,\omega) * \sum_{m=-\infty}^{\infty} J_m(\delta_{\mathrm{M2}})\delta(\omega - m\omega_{\mathrm{M2}}) . \quad (63)$$

The second grating of the second dimension G4 now acts to disperse the increased bandwidth and removes the preshear from the grating G3. Let the linearized angular dispersion be of equal magnitude to the grating G3 but with opposite sign, i.e., $+\xi_x$, so that the electric field becomes

$$E_{\mathrm{G4}}(\mathbf{r}_T,t) = E_{\mathrm{M2}}(\mathbf{r}_T,t-\xi_x x) \quad (64)$$

and the unsheared angular spectrum is given by

$$\tilde{E}_{\mathrm{G4}}(\mathbf{k}_T,\omega) = \tilde{E}_{\mathrm{M2}}(k_x+\xi_x\omega,k_y,\omega) . \quad (65)$$

After substituting the results of Eqs. (52), (55), (57), and (60),

$$E_{\mathrm{G4}}(\mathbf{r}_T,t) = E_{\mathrm{G3}}(\mathbf{r},t+\xi_x x)e^{i\delta_{\mathrm{M2}}\sin[\omega_{\mathrm{M2}}(t+\xi_x x)]}$$
$$= E_{\mathrm{G2}}(\mathbf{r}_T,t)e^{i\delta_{\mathrm{M2}}\sin[\omega_{\mathrm{M2}}(t+\xi_x x)]}$$
$$= E_0(\mathbf{r}_T,t)e^{i\delta_{\mathrm{M1}}\sin[\omega_{\mathrm{M1}}(t+\xi_y y)]}e^{i\delta_{\mathrm{M2}}\sin[\omega_{\mathrm{M2}}(t+\xi_x x)]}$$
$$= E_0(\mathbf{r}_T,t)\sum_{l=-\infty}^{\infty} J_l(\delta_{\mathrm{M1}})e^{il\omega_{\mathrm{M1}}(t+\xi_y y)}$$
$$\times \sum_{m=-\infty}^{\infty} J_m(\delta_{\mathrm{M2}})e^{im\omega_{\mathrm{M2}}(t+\xi_x x)} . \quad (66)$$

Equation (66) represents a generalization of Ref. 3, which includes beam shape. The angular spectrum of the 2-D SSD operation is then given by the spatiotemporal Fourier-Laplace transform of Eq. (66):

$$\tilde{E}_{\mathrm{G4}}(\mathbf{k}_T,\omega) = \tilde{E}_0(\mathbf{k}_T,\omega)$$
$$* \sum_{l=-\infty}^{\infty} J_l(\delta_{\mathrm{M1}})\delta(k_x, k_y - l\xi_y\omega_{\mathrm{M1}}, \omega + l\omega_{\mathrm{M1}})$$
$$* \sum_{m=-\infty}^{\infty} J_m(\delta_{\mathrm{M2}})\delta(k_x - m\xi_x\omega_{\mathrm{M2}}, k_y, \omega + m\omega_{\mathrm{M2}})$$
$$= \tilde{E}_0(\mathbf{k}_T,\omega) * \sum_{l=-\infty}^{\infty}\sum_{m=-\infty}^{\infty}\left[J_l(\delta_{\mathrm{M1}})J_m(\delta_{\mathrm{M2}})\right.$$
$$\left.\times\delta(k_x - m\xi_x\omega_{\mathrm{M2}}, k_y - l\xi_y\omega_{\mathrm{M1}}, \omega + l\omega_{\mathrm{M1}} + m\omega_{\mathrm{M2}})\right], \quad (67)$$

where it is important to notice that exact replicas of the original spectrum, modified only by the amplitudes of the Bessel functions of the first kind $J_l(\delta_{\mathrm{M1}})$ and $J_m(\delta_{\mathrm{M2}})$, are centered on a regularly spaced grid or field of delta functions formed by the innermost convolution operation. The field of delta functions lies on the plane $k_x/\xi_x + k_y/\xi_y = \omega$ in the 3-D spatiotemporal spectrum and are spaced by $\xi_y\omega_{\mathrm{M1}}$ in the direction of the k_y axis, by $\xi_x\omega_{\mathrm{M2}}$ in the direction of the k_x axis, and by linear combinations of both ω_{M1} and ω_{M2} in the direction of the ω axis. Notice that there exist sum and difference frequencies, which is characteristic of two-tone phase modulation (see Ref. 14, pp. 233–234). An example of a two-tone phase-modulated temporal spectrum is illustrated in Fig. 78.8(b) for the parameters $\delta_{\mathrm{M1}} = 6.15$, $\nu_{\mathrm{M1}} = 3.3$ GHz, $\delta_{\mathrm{M2}} = 13.5$, and $\nu_{\mathrm{M2}} = 3.0$ GHz.

Spatiotemporal cross sections of a 2-D SSD pulsed laser beam with the instantaneous wavelength overlay is shown in Fig. 78.13 for two orthogonal directions for the system parameters $\delta_{\mathrm{M1}} = 6.15$, $\nu_{\mathrm{M1}} = 3.3$ GHz, $\Delta\lambda_{\mathrm{M1}} = 1.5$ Å, $\delta_{\mathrm{M2}} = 13.5$, and $\nu_{\mathrm{M2}} = 3.0$ GHz, $\Delta\lambda_{\mathrm{M2}} = 3.0$ Å, $\tau = 1$ ns, $D_y = D_x = 44$ mm, and where hyperbolic-tangent profiles were used in the spatial and temporal dimensions. At any particular moment in time, the resultant dispersed spectrum from the first dimension of the 2-D SSD operation is seen displayed across the beam as a smaller window of color (relative to the overall bandwidth). As time progresses, the window of color is swept across the total bandwidth. The number of color cycles of the second SSD dimension is given by

$$N_{c_x} \equiv \tau_{D_x}\nu_{M2} , \quad (68)$$

where $\tau_{D_x} = \xi_x D_x$. The brick of light can also be sliced in another direction, i.e., a spatial cross section at a particular instant of time that illustrates how the instantaneous colors move across the beam profile as time changes. Two examples of the 3-D intensity profile of the beam, as viewed from above, are illustrated in Fig. 78.14 with an instantaneous wavelength overlay. The color center is seen to move across the beam. The number of color cycles in each direction is readily observed.

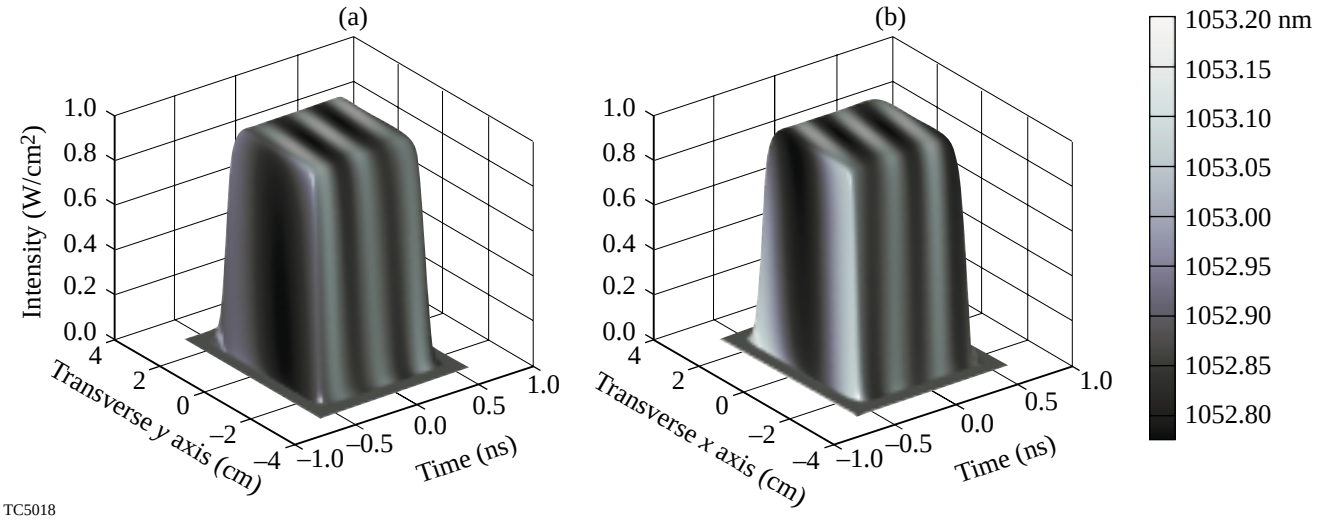

Figure 78.13
Spatiotemporal slices along (a) the *y*-*t* plane and (b) the *x*-*t* plane of a 2-D SSD pulsed beam. with an overlay of the instantaneous wavelength $\hat{\lambda}(\mathbf{r}_T, t)$ superimposed onto the intensity profile for the system parameters: $\delta_{M1} = 6.15$, $\nu_{M1} = 3.3$ GHz, $\Delta\lambda_{M1} = 1.5$ Å, $N_{c_y} \cong 1$, $\delta_{M2} = 13.5$, and $\nu_{M2} = 3.0$ GHz, $\Delta\lambda_{M2} = 3.0$ Å, $N_{c_x} \cong 0.9$, $\tau = 1$ ns, $D_y = D_x = 44$ mm, and where hyperbolic-tangent profiles were used in the spatial and temporal dimensions.

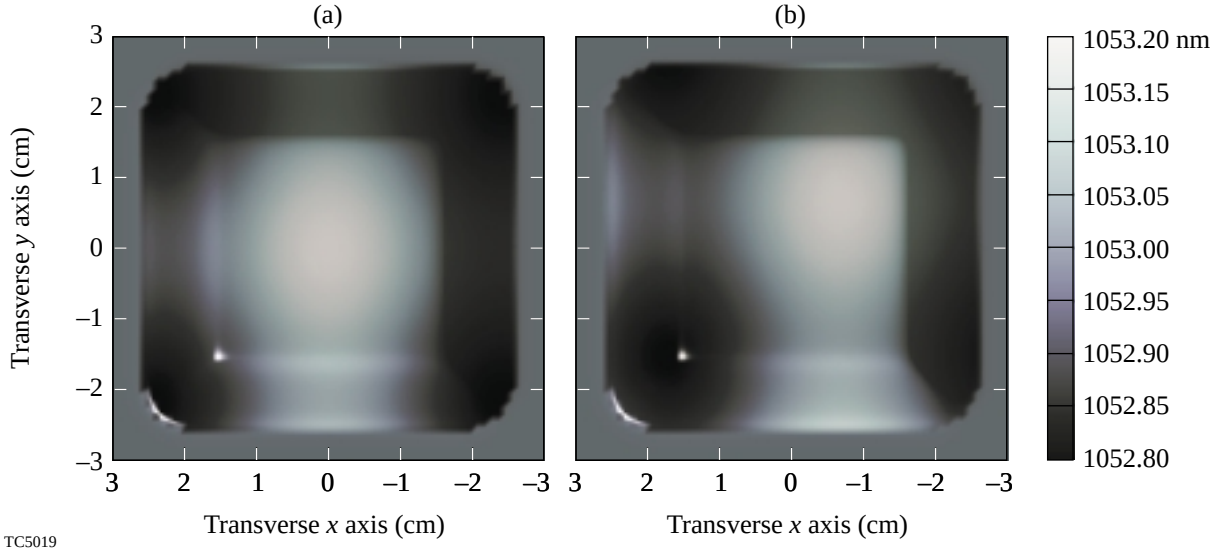

Figure 78.14
Spatial cross sections of a 2-D SSD pulsed beam with an overlay of the instantaneous wavelength $\hat{\lambda}(\mathbf{r}_T, t)$ for the system parameters: $\delta_{M1} = 6.15$, $\nu_{M1} = 3.3$ GHz, $\Delta\lambda_{M1} = 1.5$ Å, $N_{c_y} \cong 1$, $\delta_{M2} = 13.5$, and $\nu_{M2} = 3.0$ GHz, $\Delta\lambda_{M2} = 3.0$ Å, $N_{c_x} \cong 0.9$, $\tau = 1$ ns, $D_y = D_x = 44$ mm, and where hyperbolic-tangent profiles were used in the spatial and temporal dimensions. The images are for two instants of time: (a) $t_1 = 0$ ps and (b) $t_2 = 46$ ps.

A useful diagnostic for 2-D SSD systems is the time-averaged, far-field intensity structure of the pulsed beam. A far-field camera operates by propagating the 2-D SSD pulsed beam through a lens onto its focal plane, where a CCD or film captures the image in a time-integrated sense. This process takes advantage of the Fourier-transforming properties of lenses. The object is assumed to be one focal length in front of the lens (otherwise a phase curvature is imposed across the far field), and the image is in the focal plane of the lens (see Ref. 16, pp. 86–87). Waasese simulates this data by taking the time average of the expression

$$\tilde{I}_{\text{far field}}\left(\mathbf{k}_T, t\right) \equiv \frac{1}{2} n \varepsilon_0 c \left| \int\int_{-\infty}^{\infty} E_0\left(\mathbf{r}_T, t\right) e^{-i\mathbf{k}_T \cdot \mathbf{r}_T} \, \mathrm{d}x\mathrm{d}y \right|^2 . \qquad (69)$$

The expression given by Eq. (64) is equivalent to the far field in real space, at the focal plane of the lens, by making the transformations $k_x \equiv 2\pi x_{\text{ff}}/\lambda_c f$ and $k_y \equiv 2\pi y_{\text{ff}}/\lambda_c f$, where x_{ff} and y_{ff} are the real-space, far-field coordinates and f is the focal length of the lens. A time-averaged plot of Eq. (69) is illustrated in Fig. 78.15 for the same system parameters of this section. If the expression Eq. (64) is plotted directly as a function of time, a movie of the far field can be generated. The underlying far-field pattern remains constant while the spectral peaks change amplitude and can give the appearance of movement when the number of color cycles is less than 1 (provided there are no other smoothing mechanisms).

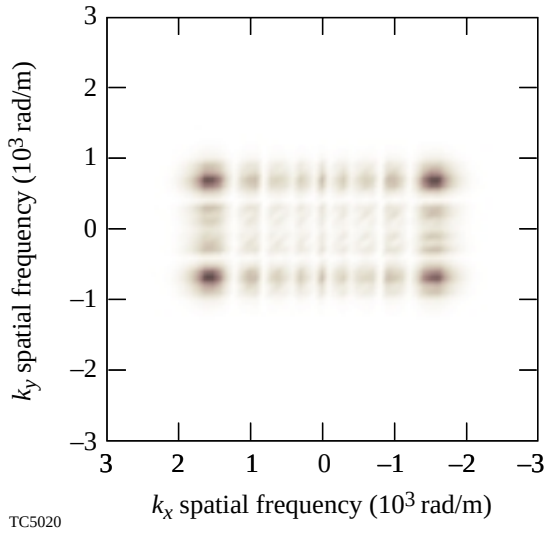

Figure 78.15
Simulation of the time-averaged far field of a 2-D SSD pulsed beam for the system parameters: $\delta_{\text{M1}} = 6.15$, $\nu_{\text{M1}} = 3.3$ GHz, $\Delta\lambda_{\text{M1}} = 1.5$ Å, $N_{c_y} \cong 1$, $\delta_{\text{M2}} = 13.5$, and $\nu_{\text{M2}} = 3.0$ GHz, $\Delta\lambda_{\text{M2}} = 3.0$ Å, $N_{c_x} \cong 0.9$, $\tau = 1$ ns, $D_y = D_x = 44$ mm, and where hyperbolic-tangent profiles were used in the spatial and temporal dimensions.

Nonideal Effects

In realistic SSD driver lines, a variety of mechanisms complicate the ideal situation described in the previous section. Some mechanisms simply distort the pulsed beam and others lead to AM. For example, if the preshear and dispersion grating are misaligned, the dispersion grating will not completely remove the distortion placed on the beam by the preshear grating. The result is a slight increase to the rise time of the pulse as well as a distorted far-field pattern in the rough shape of a rhombus. If the EO phase modulator has an angular-dependent modulation depth, the bandwidth imposed by the modulator will depend on the incident angle of the incident harmonic plane waves. This effect in combination with a grating misalignment explains the observed distorted far-field images (see Fig. 78.16); however, these two effects do not induce AM.

1. PM-to-AM Conversion Mechanisms

A variety of mechanisms destroy the ideal situation described in the previous section by producing AM. In general, they are referred to as PM-to-AM conversion mechanisms since any disruption to the spectral components of perfect phase modulation results in amplitude modulation. These mechanisms fall basically into two main categories that refer to the manner in which the spectral components can be altered: phase and amplitude effects. If the relative phases or the amplitudes of the spectral components are altered (with the exception to a linear phase variation), the phasor components will not add properly, resulting in AM. Waasese is well suited to analyze all of these effects in the spatiotemporal domain since it is based on the angular spectrum representation.

PM-to-AM conversion mechanisms further divide into temporal or spatial domain effects. Temporal domain effects directly control the phase or amplitudes by spectral filtering through devices such as etalons and amplifiers with nonconstant bandwidth. The transmissivity of etalons varies as a function of wavelength, which modulates the spectral amplitudes of a PM pulse. A similar and stronger effect is produced when a first-order ghost image co-propagates at a slight angle to the main beam, which has made one round-trip in a cavity. A streak camera measurement of this effect along with a simulation is shown in Fig. 78.17. Spatial domain effects indirectly control the spectral phase or amplitudes since, as a result of the gratings, the temporal spectrum has been coupled with the

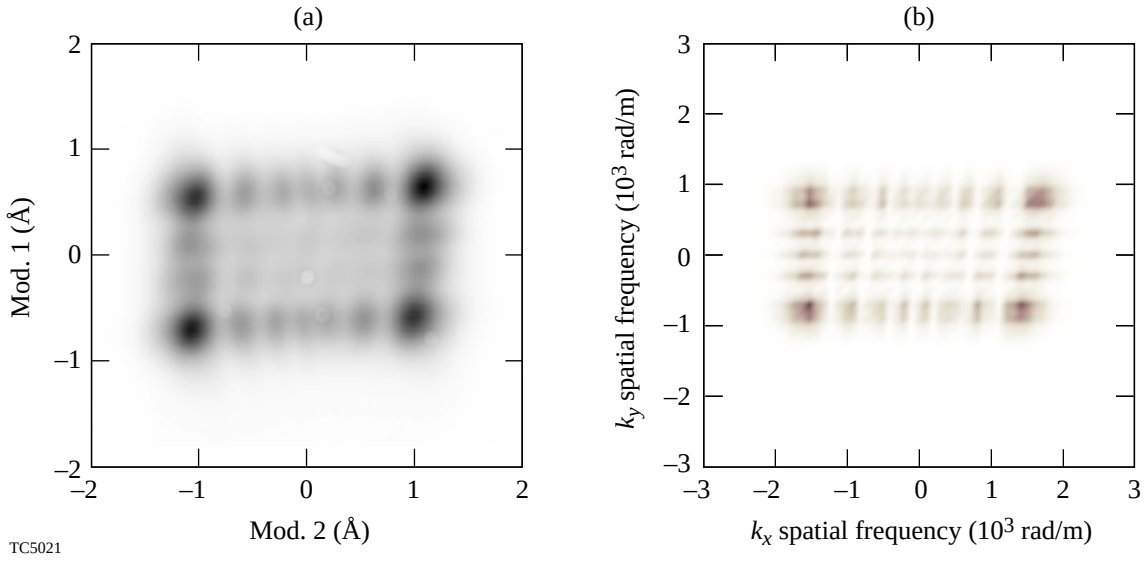

Figure 78.16
(a) A measured distorted far-field image of the double-pass 2-D SSD system and (b) a simulation of the time-averaged far field with an angular-dependent modulation depth and a G3 and G4 misalignment for the system parameters: $\delta_{M1} = 6.15$, $\nu_{M1} = 3.3$ GHz, $\Delta\lambda_{M1} = 1.5$ Å, $N_{c_y} \cong 1$, $\delta_{M2} = 13.5$, and $\nu_{M2} = 3.0$ GHz, $\Delta\lambda_{M2} = 3.0$ Å, $N_{c_x} \cong 0.9$, $\tau = 1$ ns, $D_y = D_x = 44$ mm, and where hyperbolic-tangent profiles were used in the spatial and temporal dimensions.

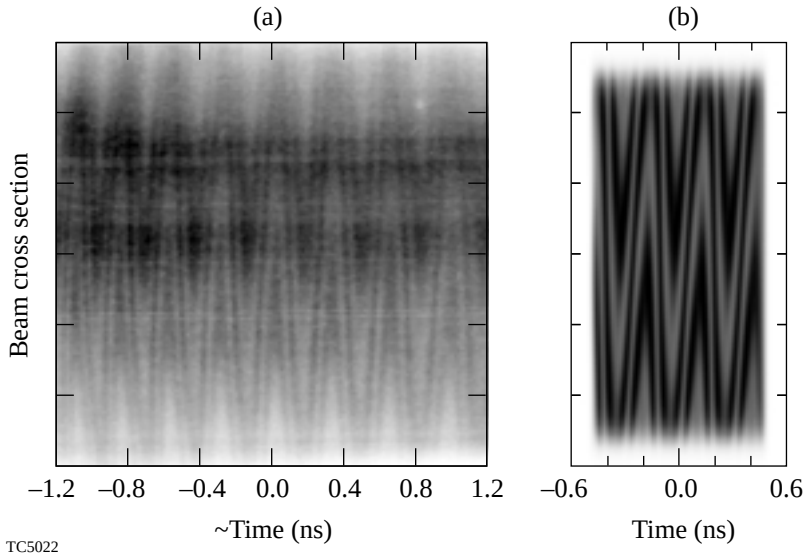

Figure 78.17
(a) A measured streak camera image (showing 2.4 ns of time) resulting from a noncollinear co-propagating reflection and (b) a simulation (showing 1 ns of time) of the interference from a first-order ghost delayed by 50 ps co-propagating at an angle of 40 μrad to the main beam. The simulation is limited to 1 ns due to practical memory constraints; however, 1 ns is sufficient to illustrate the pattern that repeats at a rate of $1/\nu_M$.

spatial spectrum, i.e., the dispersed bandwidth. Therefore, spatial domain effects play a role only after the dispersion gratings G2 of the first dimension and G4 of the second dimension and include propagation and pinhole clipping. Propagation leads to AM since each color's phase front propagates in a different direction, which imparts a different amount of phase to each color. The AM grows unbounded in a nonlinear manner as the propagation distance increases, but image relaying has the ability to restore PM at an image plane. Table 78.III contains some simulation results of propagation out of the image plane for various locations on OMEGA and for different 2-D SSD configurations. Pinhole clipping leads to AM since, in the far field, the dispersed bandwidth is splayed across the focal plane and, if the outermost colors are blocked by the pinhole, AM results.

Spatial phase variations in the near field of an SSD pulsed beam do not directly convert to AM, but the far field may be significantly broadened. If this image is passed through an image relay with a pinhole filter, spectral clipping can occur, which leads to AM. On the other hand, nonlinear spatial phase variations in the far field convert directly to AM in the near field since the spectral components are distributed in the far field as shown in Fig. 78.15. For example, surface roughness of a mirror that is placed in the far field of an image relay cavity alters the phase front of the reflected beam. Waasese simulates the surface roughness by spectrally filtering a random-number generator to match observed surface roughness statistics; an example is shown in Fig. 78.18. The effect on a 1-D SSD pulsed beam is shown in the example in Fig. 78.19. As another example, a curved retro mirror was unknowingly placed in the far-field retro stage of the second dimension and was sheared to produce planar phase fronts. When planar mirrors were substituted for the curved mirror, extremely large AM was observed. The signature of propagation out of an image plane was used to identify the AM source as a curved far-field mirror since propagation also induces a curved phase on the angular spectrum (see Fig. 78.20). Combinations of devices can also lead to AM. For example, a Faraday rotator with a wavelength-sensitive rotation in combination with a cavity ejection wave plate and a polarizer will result in an effective spectral filter.

Nonideal phase-modulator effects can be included in addition to applying the ideal PM described in Eq. (43). If the angular spectrum of the input beam is significantly broad in the direction of the optic axis, i.e., a 1-D SSD beam entering the second-dimension modulator, the crystal birefringence must

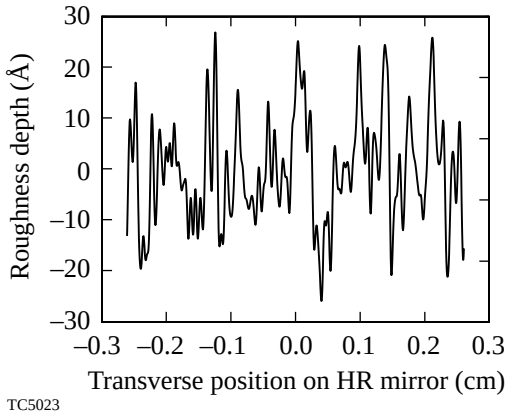

Figure 78.18
Modeled surface roughness on a far-field, high-reflecting dielectric mirror.

Table 78.III: The AM, given as a percentage of peak-to-initial value, that results from propagation out of an image plane for different locations on OMEGA and for different 2-D SSD configurations.

Component Location	Beam Diameter (cm)	1 THz N_c = 2,1 2.1, 10.4 Å 8.8, 10.2 GHz	N_c = 1,3.6 1.5, 3.0 Å 3.3, 12 GHz	N_c = 1, 1 LLNL 5.0 Å 17 GHz	N_c = 2, 1 LLNL 5.0 Å 17 GHz	Current N_c = 1, 1 1.25, 1.75 Å 3.3, 3.0 GHz
Focus lens (3ω)	27.3	13.6	31.3	2.08	8.90	5.83
FCC	27.3	0.731	1.45	0.120	0.482	0.328
F spatial filter	19.5	3.06	6.23	0.496	2.01	1.36
E spatial filter	14.6	3.88	7.98	0.626	2.55	1.72
C relay	8.49	18.9	46.1	2.81	12.3	7.91

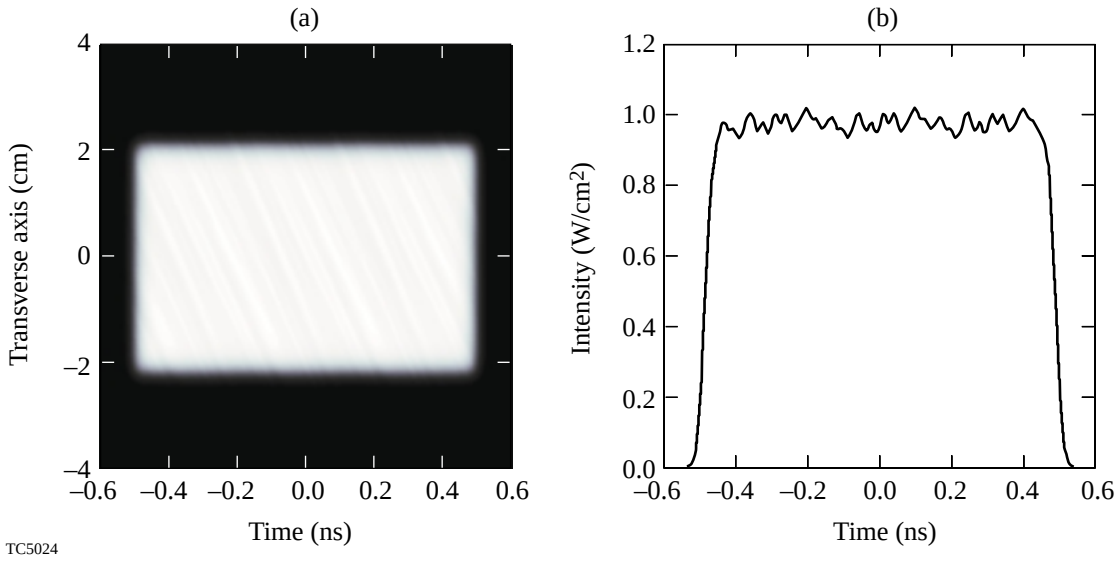

Figure 78.19
(a) Spatiotemporal cross section and (b) lineout of a 1-D SSD pulsed beam incident on a far-field mirror with surface roughness as modeled in Fig. 78.18 that yielded a peak-to-mean AM of 4.8%.

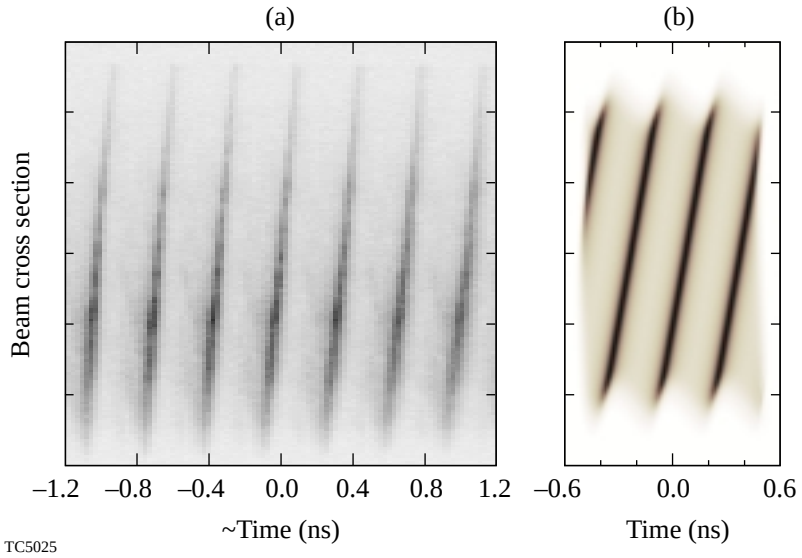

Figure 78.20
(a) A measured streak camera image (showing 3 ns of time) resulting from a phase curvature caused by an improperly placed retro mirror at the second SSD dimension double-pass cavity and (b) a simulation of the same effect, resulting in 110% peak-to-mean AM. The simulation is limited to 1 ns due to practical memory constraints; however, 1 ns is sufficient to illustrate the pattern that repeats at a rate of $1/\nu_M$.

be taken into account. This effect is exhibited by a quadratic phase distortion in the spatial frequency domain (in the direction corresponding to the optic axis) that results from the index ellipsoid of uniaxial crystals (see Ref. 17, pp. 86–90). Each harmonic plane wave produced by the first SSD dimension will experience a different phase delay as it propagates through the second modulator, which results in AM in the first dimension. Before the second dimension has been dispersed by G4, an adjustment of the image plane will correct for this AM source because propagation induces a compensating phase curvature on the angular spectrum (see Fig. 78.21). This is permissible because the spread of the angular spectrum in the second dimension is not significant before it has passed through the dispersion grating.

One other source of PM to AM is the nonlinear mapping of the grating. In the ideal case, Eq. (34) is used to describe this mapping. If the more complete nonlinear mapping is used [Eq. (17)], large enough bandwidths and color cycles will lead to a distorted mapping onto the spatial spectrum and subsequently will introduce AM. Waasese simulates this effect and shows that the distortion is greatest near the edge of the beam as seen in Fig. 78.22.

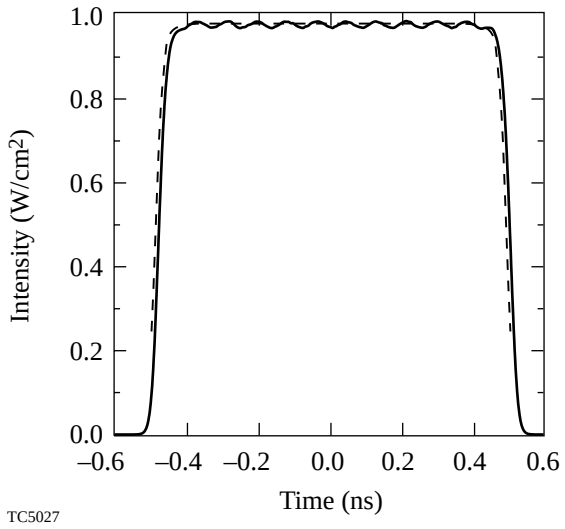

Figure 78.22
Simulation of the nonlinear grating equation effect on a 2-D SSD pulsed beam using a double-grating set. The distortion is greatest near the edge of the beam and results in a peak-to-mean AM of about 1%. The lineout is taken at $x = 1.5$ cm and $y = 0$ cm. The system parameters: $\delta_{M1} = 6.15$, $\nu_{M1} = 3.36$ GHz, $\Delta\lambda_{M1} = 1.5$ Å, $N_{c_y} \cong 1$, $\delta_{M2} = 3.38$, $\nu_{M2} = 12.06$ GHz, $\Delta\lambda_{M2} = 3.0$ Å, and $N_{c_x} \cong 3.65$.

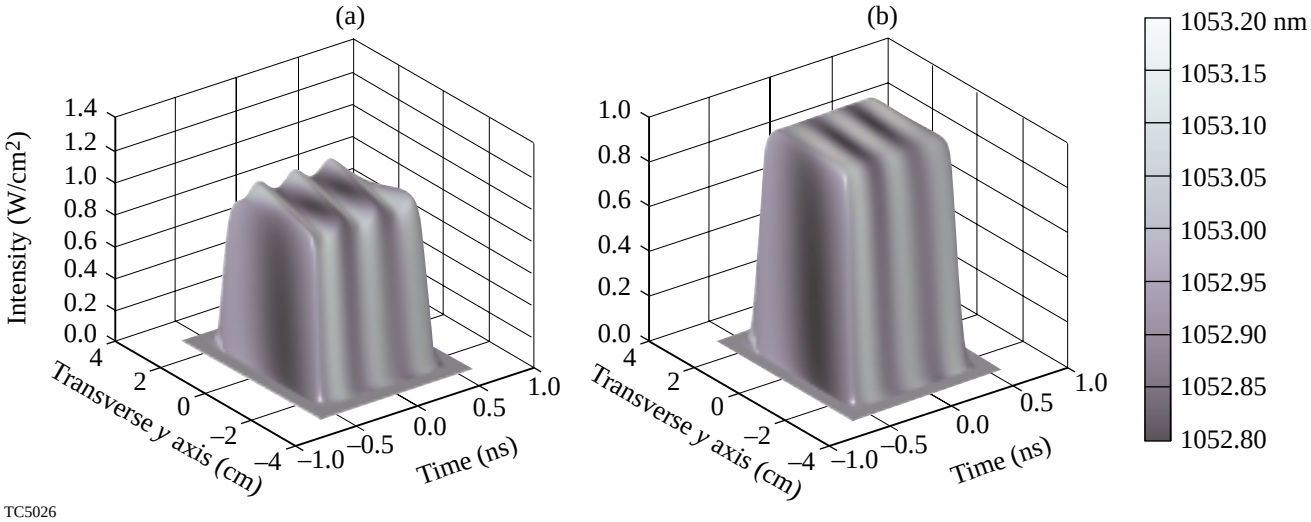

Figure 78.21
(a) Simulation of the propagation of a 1.1-mm beam through the second SSD dimension modulator while including crystal birefringence results in a peak-to-mean AM of 4%; (b) simulation of the compensating effect of a 0.56-mm adjustment to the image plane prior to the final grating at the 1.1-mm beam diameter. The system parameters: $\delta_{M1} = 6.15$, $\nu_{M1} = 3.3$ GHz, $\Delta\lambda_{M1} = 1.5$ Å, $N_{c_y} \cong 1$, $\delta_{M2} = 13.5$, and $\nu_{M2} = 3.0$ GHz, $\Delta\lambda_{M2} = 3.0$ Å, $N_{c_x} \cong 0.9$, $\tau = 1$ ns, $D_y = D_x = 44$ mm, where hyperbolic-tangent profiles were used in the spatial and temporal dimensions, and an effective $LiNbO_3$ crystal length of 36 mm.

Conclusion

Waasese provides a flexible modeling tool for simulating the generation and propagation of 2-D SSD pulsed laser beams. Waasese simulates ideal and nonideal behavior of the many optical components that comprise the SSD driver line including their relative positions. Waasese predicts measurable signatures that function as diagnostic tools since they are associated with particular optical components. The signature/component relationships act together with experimental measurements to help locate and eliminate a troublesome component. Minimizing any AM in the driver line will ensure the safety level and lifetime of OMEGA optics by circumventing the effects of small-scale self-focusing. Waasese proves to be an indispensable modeling tool for the OMEGA laser, and its inherent flexibility will provide a means to enhance its capabilities to model other laser propagation issues such as nonlinear propagation, on-target uniformity, amplifier gain, scattering losses, and pinhole clipping.

ACKNOWLEDGMENT

The authors wish to thank Dr. Jonathan Zuegel and Dr. Douglas Jacobs-Perkins for many useful discussions and laboratory work that followed. This research was supported by NSF Grant PHY94-15583. In addition, this work was partially supported by the U.S. Department of Energy Office of Inertial Confinement Fusion under Cooperative Agreement No. DE-FC03-92SF19460, the University of Rochester, and the New York State Energy Research and Development Authority. The support of DOE does not constitute an endorsement by DOE of the views expressed in this article.

REFERENCES

1. S. Skupsky, R. W. Short, T. Kessler, R. S. Craxton, S. Letzring, and J. M. Soures, J. Appl. Phys. **66**, 3456 (1989).
2. S. Skupsky and R. S. Craxton, "Irradiation Uniformity for High-Compression Laser Fusion Experiments," to be published in Physics of Plasmas.
3. Laboratory for Laser Energetics LLE Review **69**, 1, NTIS document No. DOE/SF/19460-152 (1996). Copies may be obtained from the National Technical Information Service, Springfield, VA 22161.
4. J. E. Rothenberg, J. Opt. Soc. Am. B **14**, 1664 (1997).
5. P. W. McKenty, S. Skupsky, J. H. Kelly, and C. T. Cotton, J. Appl. Phys. **76**, 2027 (1994).
6. Y. H. Chuang, L. Zheng, and D. D. Meyerhofer, "Amplification of Broad-Band Phase-Modulated Laser Pulses for Beam Smoothing by Spectral Dispersion," LLE, memorandum (August 1991).
7. R. Short, LLE, private communication (1989).
8. J. E. Rothenberg, D. F. Browning, and R. B. Wilcox, "The Issue of FM to AM Conversion on the National Ignition Facility," to be published in SPIE's Proceedings on Solid State Lasers for Application (SSLA) to Inertial Confinement Fusion, 3rd Annual International Conference, Monterey, CA, 7–12 June 1998.
9. J. A. Marozas, "Angular Spectrum Representation of Ultrawideband Electromagnetic Pulse Propagation in Lossy, Dispersive Dielectric Slab Waveguides," Ph.D. Thesis, University of Vermont, 1998.
10. K. E. Oughstun and G. C. Sherman, *Electromagnetic Pulse Propagation in Causal Dielectrics*, Springer Series on Wave Phenomena, Vol. 16 (Springer-Verlag, Berlin, 1994).
11. A. E. Siegman, *Lasers* (University Science Books, Mill Valley, CA, 1986).
12. E. G. Loewen and E. Popov, *Diffraction Gratings and Applications*, Optical Engineering, Vol. 58 (Marcel Dekker, New York, 1997).
13. Laboratory for Laser Energetics LLE Review **68**, 192, NTIS document No. DOE/SF/19460-139 (1996). Copies may be obtained from the National Technical Information Service, Springfield, VA 22161.
14. A. B. Carlson, *Communication Systems: An Introduction to Signals and Noise in Electrical Communication*, McGraw-Hill Electrical and Electronic Engineering Series (McGraw-Hill, New York, 1968).
15. M. Abramowitz and I. A. Stegun, eds. *Handbook of Mathematical Functions with Formulas, Graphs, and Mathematical Tables*, Applied Mathematics Series 55 (U.S. Government Printing Office, Washington, DC, 1964).
16. J. W. Goodman, *Introduction to Fourier Optics* (McGraw-Hill, New York, 1968).
17. A. Yariv, in *Quantum Electronics*, 2nd ed. (Wiley, New York, 1975).